Geophys. J. Int. (1992) **109**, 437–448

Antarctic marine gravity field from high-density satellite altimetry

David T. Sandwell
Scripps Institution of Oceanography, La Jolla, CA 92093, USA

Accepted 1991 November 23. Received 1991 October 21; in original form 1991 May 31

SUMMARY

Closely spaced satellite altimeter profiles (<5 km) collected during the Geosat Geodetic Mission (Geosat/GM), and those planned for the extended ERS-1 mission, are easily converted to grids of vertical gravity gradient and gravity anomaly. As profile spacing decreases, it becomes increasingly difficult to perform a crossover adjustment on the original geoid height profiles without introducing large cross-track gradients. If one is only interested in the horizontal and vertical derivatives of the gravitational potential, however, adjustment of the profile is unnecessary. The long-wavelength radial orbit error is suppressed well below the noise level of the altimeter by simply taking the along-track derivative of each profile. Ascending and descending slope profiles are then interpolated onto separate uniform grids. These two grids are summed and differenced to form comparable grids of east and north vertical deflection. Using Laplace's equation, the vertical gravity gradient is calculated directly from the vertical deflection grids. Fourier analysis is required to construct gravity anomalies from the two vertical deflection grids. These techniques are applied to high-density (~2 km profile spacing) Geosat/GM profiles in Antarctic waters (60°S to 72°S). Gridding and interpolation are performed using the method of projection onto convex sets where the smoothness criteria corresponds to upward continuation through 4 km of ocean. The resultant gravity grids have resolution and accuracy comparable to shipboard gravity profiles. After adjustment of a DC shift in the shipboard gravity profiles (~5 mGal) the rms difference between the ship and satellite gravity is 5.5 mGal. Many interesting and previously uncharted features are apparent in these new gravity maps including a propagating rift wake and a large 'leaky transform' along the Pacific–Antarctic Rise.

Key words: altimetry, Antarctic, gravity.

INTRODUCTION

Over the past decade, satellite altimetry has become an important technique for studying the geology and geophysics of remote ocean areas (Haxby *et al.* 1983; Sandwell 1984a; Haxby & Weissel 1986; Haxby 1987). Spacecraft such as Geos-3, Seasat and Geosat use pulse-limited radar, along with very accurate orbits, to measure the topography of the ocean surface which is a good approximation of the marine geoid (i.e. the equipotential ocean surface). For marine geology and geophysics applications, it is desirable to compute the gravity anomaly or vertical deflection from the geoid height. At short wavelengths (<200 km), the gravity anomaly mimics the seafloor topography. Thus these satellite altimeter data provide important reconnaissance information over vast areas of uncharted seafloor such as the Southern Ocean and Antarctic Margins. Some geophysical applications of these data include: location of uncharted features for planning detailed shipboard surveys and improving bathymetric charts (Baudry, Diament & Albouy 1987); investigation of ridge-axis morphology and isostasy (Small & Sandwell 1989); investigation of lithospheric flexure at fracture zones (Wessel & Haxby 1990) and trenches (McAdoo, Martin & Poulose 1985); identification of fracture zone trends for improving plate reconstruction models (Shaw & Cande 1990); determination of the global distribution and loading histories of undersea volcanoes (Calmant, Francheteau & Cazenave 1990); and location of marine sedimentary basins for hydrocarbon exploration (Bostrom 1989).

Until recently, the wide track spacing of the unclassified data sets was the major factor limiting the resolution of

Table 1. Altimeter capabilities.

Satellite	Precision (1μrad ≈ 1mGal)	Along-Track[1] Resolution, λ	Cross-Track[2] Resolution, λ	Date
Geos-3	30 μrad	80 km	20 - 400 km	1975
Seasat	10 μrad	50 km	80-120 km	1978
Geosat/GM[3]	6 μrad	30 km	4 km	1985
Geosat/ERM	<1 μrad	20 km	160 km	1987

[1] Along-track resolution of Geos-3, Seasat, Geosat/ERM and Geosat/GM is based on published repeat-track coherence.
[2] Cross-track resolution is twice the track spacing at the equator.
[3] Geosat/GM data north of 60°S are classified by Department of Defense

marine gravity field. In utilizing the sparse data, one could either chose to degrade its inherent along-track resolution by constructing gridded geoid/gravity anomaly maps (Haxby *et al.* 1983; Sandwell 1984a; Marsh *et al.* 1986; Freedman & Parsons 1986) or use the higher resolution profiles (Sandwell 1984b; Roest 1987) which are difficult to interpret. In any case, the major limitation of satellite altimetry is not precision or along-track resolution of the profiles, but poor coverage. In this study it is demonstrated that additional altimeter coverage leads to an order of magnitude improvement in the resolution of the marine gravity field.

Measurement capabilities for completed satellite altimeter missions are summarized in Table 1. Measurement precisions are most easily evaluated in terms of vertical deflection (i.e. sea surface slope) along individual satellite altimeter profiles. This precision depends primarily on short-wavelength (<100 km) altimeter 'noise' and to a lesser extent on intermediate-wavelength (100–1000 km) ocean variability; orbit error is not a limitation (Sandwell & Zhang 1989). It is convenient that 1 μrad of vertical deflection error translates into 0.98 mGal of gravity anomaly error. The along-track resolution of the satellite altimeter profiles is estimated by calculating the spectral coherence between independent repeat profiles (Marks & Sailor 1986; Sandwell & McAdoo 1990). Finally the cross-track resolution is twice the characteristic spacing of the profiles.

While the Geos-3 altimeter greatly exceeded its design goal, the profiles are quite 'noisy' (~30 μrad) in comparison with later missions. This low precision limits the along-track resolution to about 80 km (full wavelength). The Seasat altimeter, which operated for only three months in 1978, collected a remarkable data set having a precision of about 10 μrad (~10 mgal) and an along-track resolution of about 50 km (Marks & Sailor 1986). Unfortunately, the short lifetime of the mission resulted in poor cross-track resolution (80–120 km). Moreover, Seasat only operated during the Austral winter when sea ice obscured much of the ocean surface in Antarctic waters. The Geosat altimeter was launched by the US Navy in March 1985. Its primary (classified) geodetic mission (Geosat/GM) was to map the marine gravity field at a high spatial resolution on a global basis (see *Johns Hopkins APL Technical Digest* 1987, vol. 8). At the end of the 18 month geodetic mission, Geosat was placed into an orbit with a 17 day repeat ground track (i.e., 244 revolutions per repeat cycle) which overlies one of the 17 day Seasat ground tracks (Cheney *et al.* 1987). Many repeat profiles (up to 66) can be averaged to improve the precision, resolution and coverage of the profiles (Sandwell & McAdoo 1990). The repeatability or precision of the average Geosat profile is generally better than 1 μrad and the full-wavelength resolution is 20–24 km. While the Geosat/ERM coverage is quite uniform, large diamond-shaped gaps (~70 km) still remain so that the 2-D gravity field of the oceans is poorly resolved (160 km cross-track resolution).

Recently, high-density Geosat/GM data from the extreme southern ocean (south of −60° latitude) were declassified and are available from NOAA (McAdoo *et al.* 1991; Marks, McAdoo & Sandwell 1991). The focus of this study is on generating high-resolution gravity grids from these dense profiles (Figs 1 and 2). An independent approach to this gridding process is given by McAdoo & Marks (1992). Individual Geosat profiles have a precision of about 6 μrad and along-track resolution of about 30 km (Table 1). The close spacing of the profiles supports a cross-track resolution which is many times better than the along-track resolution. This redundancy permits construction of a 2-D gravity field with equal resolution in all directions. The objective of this study is to present a simple and accurate method of producing grids of vertical deflection, gravity anomaly and vertical gravity gradient from the altimeter profiles. The key to the processing is to avoid adjusting the DC level of the geoid profiles through a crossover adjustment.

SATELLITE GEODESY

With the dense coverage available from the Geodetic/GM, there are several reasons to avoid a crossover adjustment. First, consider two parallel tracks that are 2 km apart such as many of the tracks shown in Fig. 2. The random noise in the altitude measurement is about 30 mm (Sailor & LeSchack 1987). After a crossover adjustment, if one track is 10 mm higher than the adjacent track then a cross-track slope of 5 μrad occurs. This artificial cross-track slope will produce a stripe in the final vertical deflection or gravity maps having an amplitude of 5 mGal. The stripe could be eliminated with a low-pass filter although this reduces the resolution of the map. A second reason to avoid a crossover adjustment is also illustrated in Fig. 2. For the Geosat/GM data, the characteristic spacing of adjacent tracks is about equal to the spacing of the data points along the tracks (3.4 km). Therefore it would be a major task to locate all of the crossover points and determine their crossover differences. Moreover the size of the crossover adjustment would be enormous. Finally, and most importantly, if one is not interested in recovering geoid height then adjustment of

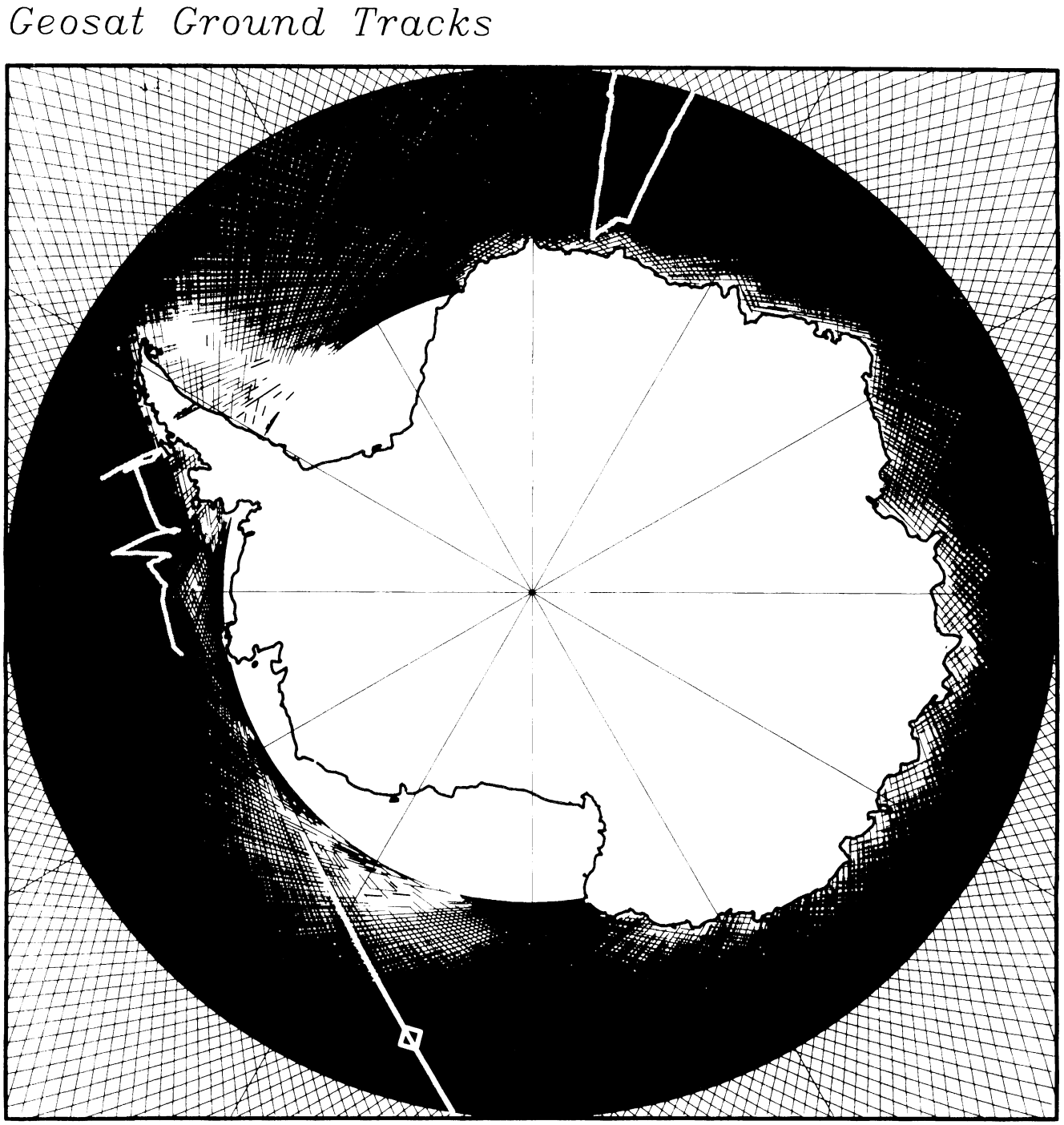

Figure 1. Tracks of Geosat altimeter profiles, collected during the 18 month geodetic mission (−60° to −72° latitude), are shown as thin lines (after editing). Exact repeat mission profiles, collected over a two-year period, are shown as intermediate lines. White box and white track mark profiles shown in Figs 2, 4 and 5. Thick grey lines are tracks of shipboard gravity shown in Fig. 8.

the profiles is completely unnecessary. As shown in many previous studies, the largest source of error in satellite altimeter profiles is the radial orbit error. The orbit error spectrum has a large peak (~5 m for Geosat) at 1 cycle per orbit (40 000 km wavelength) and a second much smaller peak (~1 m) at 2 cycles per orbit (Sandwell & Zhang 1989). If one computes the along-track slope of the profile, these radial orbit errors map into 0.8 and 0.15 μrad of slope error at once and twice per orbit respectively; such errors are well below the noise level (~6 μrad) of individual altimeter profiles (Sandwell & McAdoo 1990) and thus adjustment is unnecessary.

Vertical deflection

To avoid any adjustment of the data, ascending and descending satellite altimeter profiles are first differentiated in the along-track direction resulting in geoid slopes or

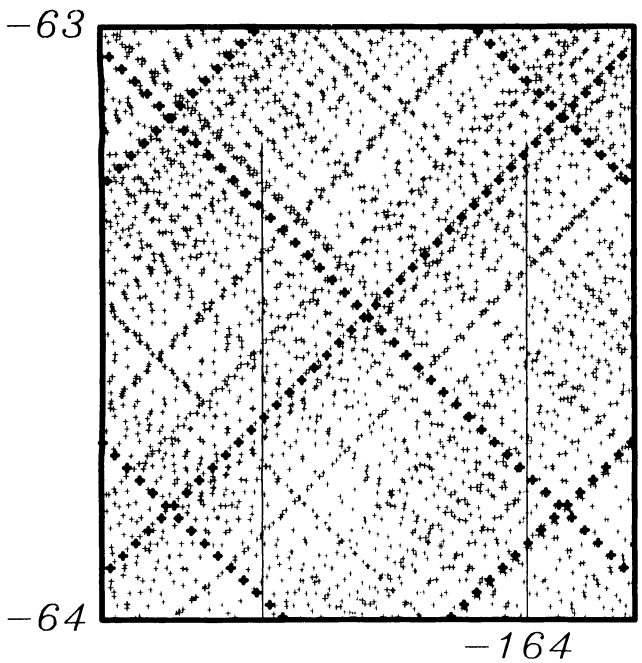

Figure 2. Typical Geosat coverage for an area 1° latitude by 2° longitude. Thin crosses are Geosat/GM observations while thick crosses are Geosat/ERM observations. See outline of area in Fig. 1.

along-track vertical deflections. These along-track slopes are then combined to produce east η and north ξ components of vertical deflection (Sandwell 1984a). Finally, the east and north vertical deflections are used to compute both gravity anomaly and vertical gravity gradient. The algorithm used for gridding the altimeter profiles is an iteration scheme (Menke 1991) relying on rapid transformation from ascending/descending geoid slopes to north/east vertical deflection and vice versa. Here I develop simple analytic formulae to perform these forward and inverse transformations. Consider for the moment the intersection point of an ascending and a descending satellite altimeter profile. The derivative of the geoid height N with respect to time t along the ascending profile is

$$\dot{N}_a \equiv \frac{\partial N_a}{\partial t} = \frac{\partial N}{\partial \theta}\dot{\theta}_a + \frac{\partial N}{\partial \phi}\dot{\phi}_a \tag{1}$$

and along the descending profile is

$$\dot{N}_d = \frac{\partial N}{\partial \theta}\dot{\theta}_d + \frac{\partial N}{\partial \phi}\dot{\phi}_d \tag{2}$$

where is θ geodetic latitude and ϕ is longitude. The functions $\dot{\theta}$ and $\dot{\theta}$ are the latitudinal and longitudinal components of the satellite ground track velocity. It is assumed that the satellite altimeter has a nearly circular orbit so that its velocity depends mainly on latitude. At the crossover point the following relationships are accurate to better than 0.1 per cent for Geos-3, Seasat and Geosat orbits:

$$\dot{\theta}_a = -\dot{\theta}_d \tag{3}$$

and

$$\dot{\phi}_a = \dot{\phi}_d. \tag{4}$$

(In the next section, simple analytic expressions are derived for these velocities.) Equations (1), (2), (3) and (4) can be combined to relate east and north vertical deflection to the along-track vertical deflections at the crossover point. The east component of geoid slope is found by adding equations (1) and (2) using (3). The result is

$$\frac{\partial N}{\partial \phi} = \frac{1}{2\dot{\phi}}(\dot{N}_a + \dot{N}_d). \tag{5}$$

Similarly the north component of geoid slope is found by subtracting (2) from (1) using equation (4):

$$\frac{\partial N}{\partial \theta} = \frac{1}{2|\dot{\theta}|}(\dot{N}_a - \dot{N}_d). \tag{6}$$

Finally, the east η and north ξ components of vertical deflection are related to the two geoid slopes (Heiskanen & Moritz 1967) by

$$\eta = -\frac{1}{a\cos\theta}\frac{\partial N}{\partial \phi}, \tag{7}$$

$$\xi = -\frac{1}{a}\frac{\partial N}{\partial \theta}, \tag{8}$$

where a is the mean radius of the earth. In a following section, equations (1), (2), (5) and (6) will be used to transform between complete grids of ascending and descending along-track geoid slopes and the corresponding grids of east and north geoid slope; collocated grid cells are analogous to crossover points (Sandwell 1984a).

It is evident from this formulation that there are latitudes where either the east or north component of geoid slope may be poorly determined. For example, at ±72° latitude, the Seasat and Geosat altimeters reach their turning points where the latitudinal velocity $\dot{\theta}$ goes to zero and thus (6) becomes singular. In theory, this is not a problem because the ascending and descending profiles are nearly paralellel so that (in the absence of noise) their difference goes to zero at the same rate as the latitudinal velocity goes to zero. Of course in practice altimeter profiles contain noise, so that the north component of geoid slope will have a signal-to-noise ratio that decreases near ±72° latitude. Similarly, for an altimeter in a near polar orbit, the ascending and descending profiles are nearly antiparallel at the low latitudes; the east component of geoid slope (5) is poorly determined and the north component is well determined. The best situation occurs when the tracks are nearly perpendicular so that the east and north components of geoid slope have the same signal-to-noise ratio.

Approximate satellite position and velocity

The exact satellite ground-track velocity could be calculated directly from the ground-track profiles supplied with the satellite altimeter data records. However, later on we will need to evaluate equations (1), (2), (5) and (6) at grid cells that were not necessarily intersected by a satellite profile. Thus it is desirable to have an accurate formula for computing $\dot{\theta}$ and $\dot{\phi}$ versus latitude.

For completeness, I derive expressions for both the appoximate position and velocity of a satellite in a circular orbit about an ellipsoidal earth. The important parameters

Table 2. Geometric parameters.

Parameter	Description	Value			
		Geos-3	Seasat	Geosat	Ers-1
ω_s	orbit freq.	1.0420×10^{-3}	1.0407×10^{-3}	1.0407×10^{-3}	1.0379×10^{-3} s^{-1}
ω_n	precession freq.	4.144×10^{-7} s^{-1}	-	-	-
I	inclination	114.980°	108.058°	108.058°	98.549°
ω_e	earth rotation freq.	7.29214×10^{-5} s^{-1}			
f	flattening	1/298.25			
a	mean earth radius	6371000 m			
g_o	accel. of gravity	9.81 m s^{-2}			

are the orbit frequency ω_s, the earth rotation rate ω_e, the precession rate of the orbit plane about the earth's spin axis ω_n, the inclination of the satellite orbit I, the longitude of the satellite ϕ, the flattening of the earth f, the geocentric latitude θ_c, and the geodetic latitude θ. Numerical values of the constant parameters are given in Table 2.

To attain the desired level of approximation, it is necessary to account for the oblateness of the earth when computing latitude and latitudinal velocity. Assuming the earth is an oblate ellipse with flattening f, the conversion from geocentric θ_c to geodetic latitude θ is

$$\tan\theta = (1-f)^{-2}\tan\theta_c. \tag{9}$$

At the equator and at the poles, the two latitudes are equal but at intermediate latitudes (e.g., 45°) they differ by up to 0.2°. The derivative of (9) with respect to time provides the correction to the latitudinal velocity when converting from the geocentric system to the geodetic system:

$$\frac{\dot\theta}{\dot\theta_c} = (1-f)^{-2}\frac{\cos^2\theta}{\cos^2\theta_c}. \tag{10}$$

Equations for the relative position of the satellite versus time were derived following Kaula (1966). The basic problem is to map the position of a satellite in a circular orbit about the earth into an earth-fixed coordinate system. Let $t=0$ be the time when the satellite orbit crosses the earth's equatorial plane on an ascending pass at a longitude of ϕ_0. To develop formulaes, one first represents the position of the satellite in a Cartesian coordinate system $\mathbf{q}$ where the q_x-axis is the line connecting the centre of the earth and the ascending equator crossing. The q_z-axis is perpendicular to the orbit plane and the q_y-axis is orthogonal to the q_x and q_z axes. In this frame, the q_x, q_y and q_z positions are $\cos(\omega_s t)$, $\sin(\omega_s t)$ and 0, respectively. Next the satellite frame is rotated about the q_x-axis by the inclination of the orbit plane relative to the earth's equatorial plane I. A third rotation about the earth's spin axis maps the satellite plane into an earth-fixed system. This final rotation involves the rotation rate of the earth relative to the precessing orbit plane $\omega_e' = \omega_e - \omega_n$. After performing the three rotations and transforming the results from Cartesian coordinates into spherical coordinates, one obtains expressions for the latitude and longitude versus time. The geocentric latitude is

$$\theta_c(t) = \sin^{-1}(\sin\omega_s t\sin I). \tag{11}$$

This geocentric latitude is converted to geodetic latitude using equation (9). In addition, (11) can be inverted to yield the time since the equator crossing:

$$t(\theta_c) = \omega_s^{-1}\sin^{-1}\left(\frac{\sin\theta_c}{\sin I}\right). \tag{12}$$

The cosine and sine of the longitude (relative to ϕ_0) at some later time are given by

$$\cos\phi(t) = \left(\frac{\cos\omega_e' t\cos\omega_s t + \sin\omega_e' t\sin\omega_s t\cos I}{\cos\theta_c(t)}\right) \tag{13}$$

and

$$\sin\phi(t) = \left(\frac{-\sin\omega_e' t\cos\omega_s t + \cos\omega_e' t\sin\omega_s t\cos I}{\cos\theta_c(t)}\right). \tag{14}$$

By combining these two expressions, the longitude at a later time is

$$\phi(t) = \tan^{-1}\left(\frac{-\sin\omega_e' t\cos\omega_s t + \cos\omega_e' t\sin\omega_s t\cos I}{\cos\omega_e' t\cos\omega_s t + \sin\omega_e' t\sin\omega_s t\cos I}\right) + \phi_0. \tag{15}$$

Although equations (11)–(15) are not used in this paper, they are extremely useful for accumulating repeating satellite altimeter profiles into uniform along-track bins (Sandwell & McAdoo 1990).

Given these equations for position versus time, one can derive expressions for the latitudinal and longitudinal component of the satellite velocity versus latitude. The latitudinal velocity is obtained by differentiating (11) with respect to time and using (12) to relate velocity to latitude instead of time. The result is

$$\dot\theta_c(t) = \omega_s\left(1-\frac{\cos^2 I}{\cos^2\theta_c}\right)^{1/2}. \tag{16}$$

Of course, the sign of the velocity will depend on whether the satellite profile is ascending (+) or descending (−). To convert from geocentric velocity to geodetic velocity, equation (10) is used. The longitudinal velocity of the satellite is most easily determined by using the fact that the total angular velocity of the satellite (in the satellite frame) is constant (ω_s). Then the longitudinal velocity of the satellite relative to the earth is

$$\dot\phi = \omega_s\frac{\cos I}{\cos^2\theta_c} - \omega_e'. \tag{17}$$

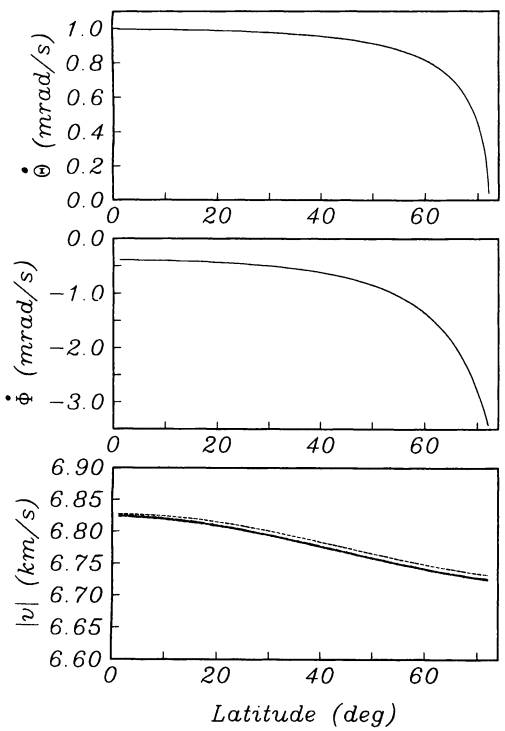

Figure 3. Latitude component (top) of Geosat ground track velocity versus latitude (solid line—observations, dashed line—theory). Longitude component (middle) of Geosat ground track velocity versus latitude (solid—observations, dashed—theory). Total ground track speed (bottom) for Geosat (solid—observed, dashed—theory); the largest difference is 7 m s^{-1}.

To establish the accuracy of these approximate satellite velocities, equations (16) and (17) were compared with the trajectory of a Geosat Exact Repeat Mission profile (Cheney *et al.* 1987). The observed latitudinal, longitudinal and total velocities (Fig. 3, top, middle and bottom, solid curves) were computed by numerical differentiation of a Geosat/ERM profile between 0° and 72° south latitude. The latitudinal velocity decreases from about 1.0 mrad s^{-1} at the equator to zero at 72°. The longitudinal velocity is negative since Geosat has an inclination of 108°; its magnitude increases from 0.4 mrad s^{-1} at the equator to 3.4 mrad s^{-1} at the turning points ±72°. The dashed curves shown in Fig. 3 are the velocities computed using equations (9), (10), (16) and (17). Results show that the model velocities lie within 1 μrad s^{-1} of the actual velocities. The greatest error in total velocity occurs at 72° latitude where the difference is 7 m s^{-1} or 0.1 per cent. Other numerical tests (not presented here) show that the position estimates from equations (11) and (15) are accurate to better than 1 km as long as the predicted position is less than 1/4 an orbit from the known equator crossing position.

Gravity gradient and gravity anomaly

In the next section, complete grids of east and north vertical deflection are constructed from a dense network of Geosat Geodetic Mission profiles (McAdoo *et al.* 1991). Here the theory for converting gridded maps of vertical deflection into vertical gravity gradient and gravity anomaly is presented. The gravity gradient computation turns out to be simple numerical differentiation of the vertical deflection grids and does not involve any assumptions. However, to construct gravity anomalies from vertical deflections, either a spherical harmonic expansion or a Fourier expansion must be used. Rapp & Pavlis (1990) have used the spherical harmonic approach complete to degree and order 360 (111 km wavelength) for construction of a globally accurate gravity field. The focus of this study is not global accuracy but high spatial resolution (<25 km wavelength) for regional maps. Thus the Fourier transform method described briefly in Haxby *et al.* (1983), Freedman & Parsons (1986) and McAdoo (1990) is used to convert gridded vertical deflections into gravity anomalies. Of course, this approach is based on a flat-earth approximation. However, the error due to this assumption can be minimized by first removing a spherical harmonic model (e.g. degree 40) from the profiles before the gridding and construction of east and north vertical deflections. Later on, this model is added back to the gridded gravity anomaly map. Here the overall method is described in detail.

To begin, one must relate the geoid height $N(\mathbf{x})$ and other measurable quantities such as gravity anomaly $\Delta g(\mathbf{x})$ to the gravitational potential $V(\mathbf{x}, z)$. All of these quantities are deviations from some reference earth model such as a spherical harmonic expansion. In the following equations, the bold $\mathbf{x}$ denotes the coordinate (x, y); similarly $\mathbf{k}$ denotes (k_x, k_y) where $k_x = 1/\lambda_x$, where λ_x is wavelength. To a first approximation, the geoid height is related to the gravitational potential by Brun's formula,

$$N(\mathbf{x}) \cong \frac{1}{g_0} V(\mathbf{x}, 0), \tag{18}$$

the gravity anomaly is the vertical derivative of the potential,

$$\Delta g(\mathbf{x}) = -\frac{\partial V(\mathbf{x}, 0)}{\partial z}, \tag{19}$$

the east component of vertical deflection is the slope of the geoid in the x-direction,

$$\eta(\mathbf{x}) \equiv -\frac{\partial N}{\partial x} \cong \frac{-1}{g_0}\frac{\partial V}{\partial x}, \tag{20}$$

and the north component of vertical deflection is the slope of the geoid in the y-direction,

$$\xi(\mathbf{x}) \equiv -\frac{\partial N}{\partial y} \cong \frac{-1}{g_0}\frac{\partial V}{\partial y}. \tag{21}$$

These quantities are related to one another through Laplace's equation:

$$\frac{\partial^2 V}{\partial x^2} + \frac{\partial^2 V}{\partial y^2} + \frac{\partial^2 V}{\partial z^2} = 0. \tag{22}$$

Substitution of (19), (20) and (21) into Laplace's equation (22) yields a relationship between the vertical gravity gradient and the sum of the x and y derivatives of the east and north vertical deflection:

$$\frac{\partial \Delta g}{\partial z} = -g_0\left(\frac{\partial \eta}{\partial x} + \frac{\partial \xi}{\partial y}\right). \tag{23}$$

This expression is used below to compute vertical gravity gradient from grids of east and north vertical deflection. Note that this is a local computation which does not involve spherical harmonics or Fourier transforms. Indeed, given two orthogonal satellite altimeter profiles, the vertical gravity gradient at their intersection point is the sum of the curvatures of each profile times the average acceleration of gravity. The simplicity of this calculation is particularly desirable for computing the gravity gradient near coastlines where the altimeter profiles terminate; the calculation of the vertical gravity gradient from (22) has no edge effect while the Fourier computation of the gravity field can have a significant edge effect.

In contrast to the simple formulation of the gravity gradient, computation of the gravity anomaly is much more difficult and error prone. Following Haxby *et al.* (1983) the differential equation (22) is reduced to an algebraic equation by Fourier transformation. The forward and inverse Fourier transforms are defined as

$$F(\mathbf{k}) = \int_{-\infty}^{\infty}\int_{-\infty}^{\infty} f(\mathbf{x})e^{-i2\pi(\mathbf{k}\cdot\mathbf{x})}\, d^2\mathbf{x}, \tag{24}$$

$$f(\mathbf{x}) = \int_{-\infty}^{\infty}\int_{-\infty}^{\infty} F(\mathbf{k})e^{i2\pi(\mathbf{k}\cdot\mathbf{x})}\, d^2\mathbf{k}. \tag{25}$$

The Fourier transform of equation (23) is

$$\frac{\partial \Delta g(\mathbf{k}, z)}{\partial z} = -i2\pi g_0[k_x\eta(\mathbf{k}) + k_y\xi(\mathbf{k})]. \tag{26}$$

From the solution to Laplace's equation in the wavenumber domain the upward continuation formula relates the gravity anomaly at the surface of the earth to the gravity anomaly at some elevation z:

$$\Delta g(\mathbf{k}, z) = \Delta g(\mathbf{k}, 0)e^{-2\pi|\mathbf{k}|z}, \tag{27}$$

where $|\mathbf{k}| = \sqrt{k_x^2 + k_y^2}$.

Taking the derivative of (27) with respect to z and evaluating the result at $z = 0$ one arrives at an algebraic formula relating the Fourier transform of the gravity anomaly to the sum of the Fourier transforms of the two components of vertical deflection:

$$\Delta g(\mathbf{k}, 0) = \frac{ig_0}{|\mathbf{k}|}[k_x\eta(\mathbf{k}) + k_y\xi(\mathbf{k})]. \tag{28}$$

To compute gravity anomalies from a dense network of satellite altimeter profiles of geoid height, one constructs a grids of east η and north ξ vertical deflection. The grids are then Fourier transformed using a discrete approximation to (24). Finally, one performs the multiplications given in (28) and inverse Fourier transforms the result to obtain the gravity anomaly. At this point one could also add the spherical harmonic gravity model back to the gridded gravity values in order to recover the long-wavelength gravity field.

DATA PROCESSING AND POCS INTERPOLATION

Editing

Gridded gravity fields were based on the Geosat altimeter profiles collected over a 3.5 yr period including 1.5 yr of Geosat/GM profiles and 2.0 yr of Geosat/ERM profiles (Figs 1 and 2). Dense coverage is only available between −60° and −72° latitude where sea ice obscures much of the ocean surface during the Austral winter. Pack ice and large icebergs commonly corrupt the altimeter measurements so that the data must be carefully edited prior to interpolation. For the Geosat/ERM profiles, the editing and averaging sequence is described in an earlier paper (Sandwell & McAdoo 1990). The basic steps were to first edit bad points based on parameters provided with the geophysical data records (Cheney *et al.* 1987). After this preliminary edit, a subset of the corrections were applied, the profiles were differentiated along track, and the profiles were interpolated into uniform along-track bins. A second edit was performed during the averaging of the repeat cycles by testing the deviation of the individual cycle from the average. An example of a vertical deflection profile across the Pacific–Antarctic rise is shown in Fig. 4. The upper plot shows 39 individual repeat cycles that were combined to form the average vertical deflection profile (thick line). The variations in the lengths of the individual repeat cycles reflect the seasonal extent of the sea ice cover. The lower plot is the uncertainty of the average profile. It was calculated by dividing the standard deviation of the profiles about the mean profile divided by the square root of the

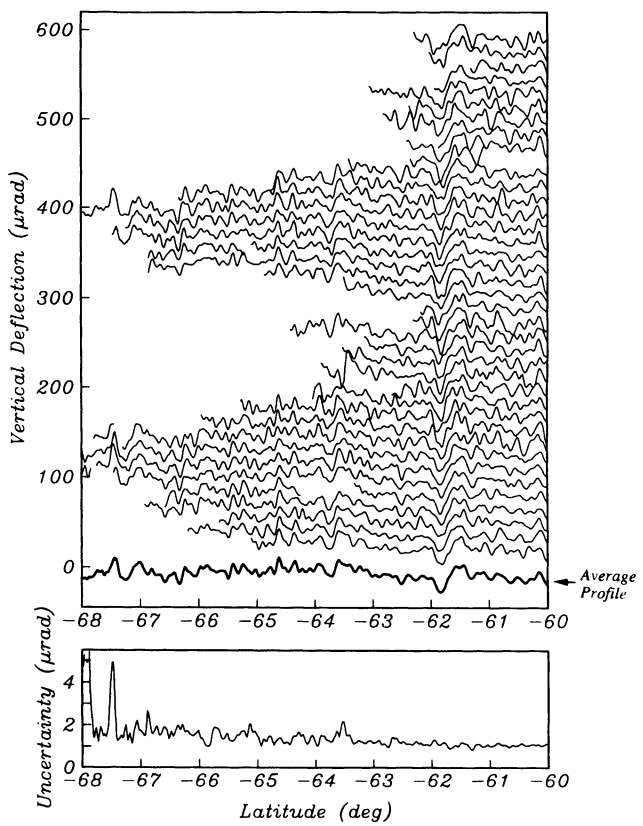

Figure 4. 40 ascending vertical deflection profiles (upper) from Geosat/ERM were averaged to improve accuracy, resolution and coverage (track location shown in Fig. 1). Most gaps are due to seasonal variations in ice cover. Uncertainty (lower) is the rms deviation from the average profile divided by the square root of the number of repeat profiles. Uncertainty is less than 1 μrad between −63° and −60° but increases at lower latitudes due to data gaps.

number of profiles in the average. Above −62° latitude the uncertainty is about 1 μrad while to the south the uncertainty increases.

A similar process was used to prepare the Geosat/GM profiles. Points were edited when the standard deviation of the 10 per second average exceeded 0.1 m as described in Cheney *et al.* (1987). Points were also edited when the significant wave height exceeded 8.0 m. Of the 6093 604 observations available (2 Hz sampling), about 50 per cent were edited resulting in 3021 237 acceptable data points. After editing, the surviving data points were corrected for the effects of solid earth tide, ocean tide, wet troposphere (FNOC), dry troposphere, and ionosphere. The final step was to divide the data into ascending and descending profiles and to differentiate each profile using the first difference formula. An example of ascending Geosat/GM profiles crossing the Pacific–Antarctic Rise is shown in Fig. 5. These profiles lie within 10 km of the Geosat/ERM profile shown in Fig. 4. The upper plot shows the geoid height profiles relative to a spherical harmonic geoid model complete to degree and order 40 (Marsh *et al.* 1990). The differences in DC level among the geoid height profiles reflect radial orbit error. The lower plot shows the along-track vertical deflection profiles. As stated above, the differentiation effectively removes the long-wavelength orbit error so that only the short-wavelength altimeter noise is apparent.

Despite the severe editing described above, a few outliers remained in the Geosat/GM data so that additional editing was necessary. As in the case of the Geosat/ERM profiles,

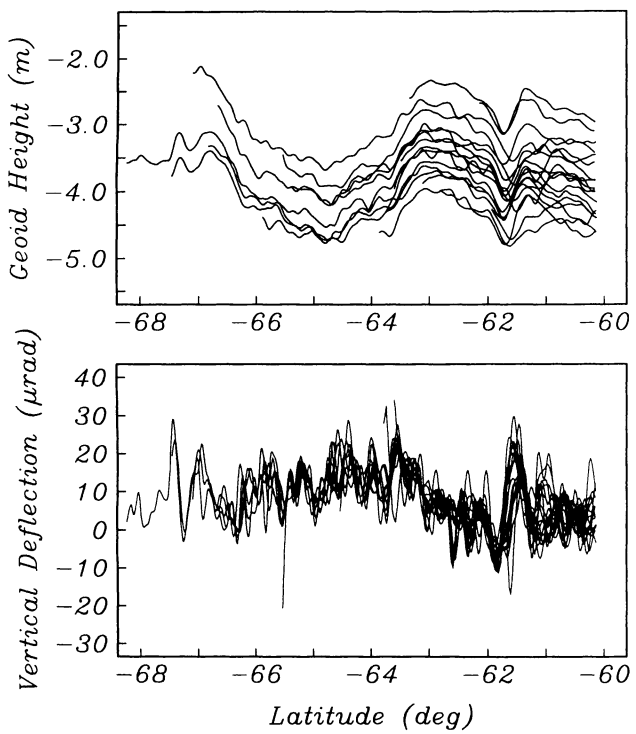

Figure 5. Geosat/GM profiles within 10 km of the Geosat/ERM profile shown in Fig. 4. The long-wavelength orbit error in the geoid height profiles (upper) appears as a DC shift among the profiles. After differentiation (lower), the long-wavelength error is suppressed below the noise level.

the secondary edit was performed by comparing individual observations with the average of nearby observations. To accomplish this, all of the ascending profiles were averaged into Mercator cells having a spacing of 1/12° in longitude and 1/12° cos θ in latitude. At −60° latitude these cells are 4.6 km by 4.6 km. An interpolating filter with a cut-off wavelength of 34 km (half-amplitude) was then applied to the array. Individual observations were edited when they differed from the smoothed grid by more than 15 μrad.

POCS interpolation

A new approach, based on the projection onto convex sets method (POCS) (Menke 1991) was used to interpolate the Antarctic Geosat profiles onto a uniform Mercator grid. The objective was to construct two uniform grids of along-track vertical deflection, $\dot{N}_a$ and $\dot{N}_d$, that can be combined to compute east and north grids of vertical deflection (equations 5 and 6). Once constructed, these grids were used to compute vertical deflections (equations 7 and 8), the vertical gravity gradient (equation 23) and the gravity anomaly (equation 28). The interpolated 'gravity field' should satisfy three conditions; it should match the ascending vertical deflection observations $\dot{N}_a$, it should match the descending observations $\dot{N}_d$, and it should be smooth. The smoothness requirement is due to the attenuation of the short-wavelength gravity components because of upward continuation from the seafloor to the sea surface. If the mean ocean depth is s, then at short wavelengths the amplitude spectrum of the gravity field should decrease as $e^{-2\pi|\mathbf{k}|s}$ where $|\mathbf{k}|$ is the magnitude of the wavenumber in equation (27). A simple method of achieving this spectral constraint is to convolve the interpolated 'gravity field' with the inverse Fourier transform of the upward continuation filter $f(r)$:

$$f(r) = \frac{1}{2\pi(s^2 + r^2)^{3/2}}, \tag{29}$$

where r is distance. The POC method is a simple and efficient method of constructing a 'gravity field' that satisfies the three constraints. The iteration sequence involves the following steps.

(1) Average the along-track vertical deflection profiles into two Mercator arrays, one for ascending profiles and the second for descending profiles. Place any reasonable value in all bins not intersected by a profile.

(2) Add and substract the two arrays as prescribed in equations (5) and (6) to form east and north slope arrays. Scale the arrays using (7) and (8).

(3) Convolve the east and north vertical deflection arrays with the upward continuation filter (29).

(4) Combine the east and north arrays as prescribed by equations (1) and (2) to recover smoothed ascending and descending along-track vertical deflection arrays.

(5) Using the original observations, reset bins that were intersected by a Geosat profile(s). Do not change the values of the other bins.

(6) Return to step 2.

After about four iterations this procedure converges to a 'gravity model' having the three desired properties. It is best

to exit from the algorithm after step 3 so the gravity field will not have discontinuities. The only parameter in the iteration scheme is the mean ocean depth; a reasonable value of 4 km was used.

ANTARCTIC MARINE GRAVITY

The POCS interpolation method was applied to the ascending and descending Geosat profiles shown in Fig. 1. The basic processing sequence was as follows. (1) Remove a spherical harmonic model complete to degree 40 (Marsh *et al.* 1990) from the ascending and descending along-track vertical deflections. (2) Average the slope profiles into two separate Mercator grids. The northern and southern edges of the grids were extended by 2° and the eastern and western edges overlapped by 10° with adjacent grids. Cosine tapers were applied to the edges. (3) Interpolate the empty grid cells using the POC method and construct grids of east and north vertical deflection. (4) Differentiate the east and north vertical deflection grids and apply equation (23) to construct a grid of vertical gravity gradient. (5) Construct the gravity anomaly using equation (28). At this point, the long-wavelength gravity anomaly was computed from the spherical harmonic coefficients and this field was added to the gravity grid.

The results are shown in Figs 6 and 7. For the gravity images (Fig. 6), the hue range from violet to orange represents gravity anomaly ranging from −35 to 35 mgal; shading is used to highlight the small-scale features. For the vertical gravity gradient (Fig. 7), the violet to orange in hue represents variations from −10 to +25 Eötvös (1 Eötvös is $10^{-9}\,s^{-2}$ or 0.1 mGal per km elevation change). In most areas, the gravity field is well resolved by the Geosat profiles and there are no indications of artificial stripes oriented in the direction of the satellite profiles. There are a few areas where the gravity field appears to be noisy. These areas coincide with poor data coverage in the Amundsen Sea (−70° to −72° latitude, −170° to −130° longitude) and the Weddell Sea (−64° to −72° latitude, −60° to −45° longitude).

Comparison with shipboard gravity

To obtain an estimate of the accuracy and resolution of the Geosat gravity grids, two ordinary shipboard gravity profiles were selected for comparison. These profiles were obtained from a data set compiled by Wessel & Watts (1988) using GeoBase software (Menke *et al.* 1991). The first profile (thb80) was acquired by a Japanese Ship in January and February of 1981. The trackline of the ship crosses the sharp gravity high associated with a now extinct convergent margin on the west side of the Antarctic Peninsula (Fig. 1, thick grey line). Gravity anomaly versus distance along the ship track is shown in Fig. 8(a) (solid curve) along with the gravity values interpolated from the Geosat gravity grid (Fig. 6e). There is a systematic DC offset of the shipboard gravity relative to the Geosat gravity of 6.6 mGal. Wessel & Watts (1988) observed similar offsets between shipboard measurements and satellite measurements in the southern hemisphere. After correcting for this DC offset, the rms difference between the two profiles is 5.7 mGal.

The second profile, acquired by the Eltanin in early 1977

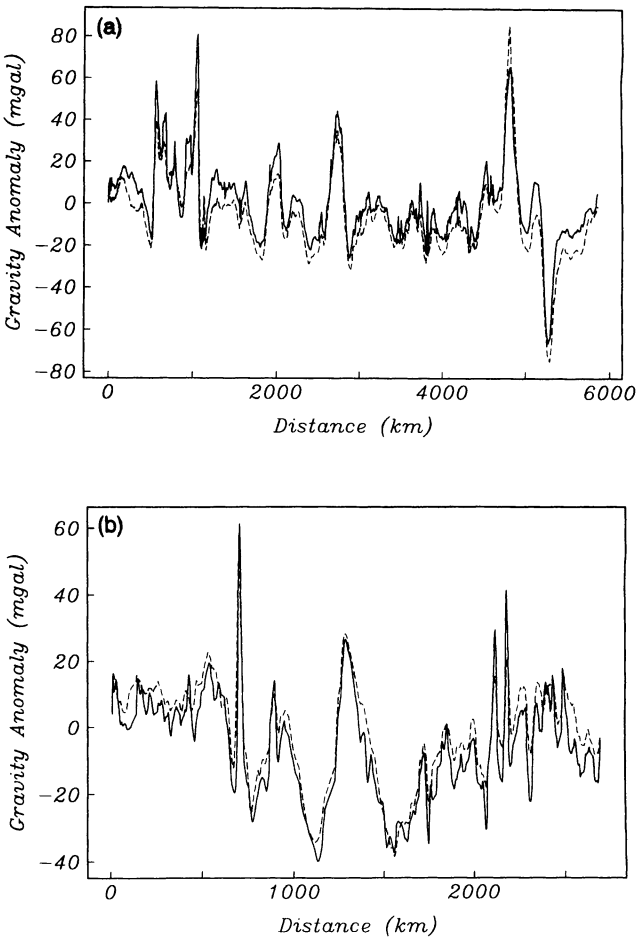

Figure 8. Comparison of shipboard gravity measurements (solid curves) and Geosat gravity grids (dashed curves) from Fig. 6. Profile (a) was acquired on the west side of the Antarctic Peninsula while profile (b) was acquired in the southern Indian ocean.

(il277), crosses the Astrid and DuToit fracture zones. In this case the shipboard gravity was systematically lower than the Geosat gravity field by 4.63 mGal and the rms difference after correcting the DC offset was 5.31 mGal. Through a crossover analysis, Wessel & Watts (1988) estimated that this gravity profile should be shifted upward by 4.70 mGal which would bring it into perfect agreement with the Geosat gravity field.

In both comparisons, the rms difference between the shipboard gravity and the Geosat gravity was about 5.5 mGal. Without additional measurements it is impossible to determine which profile is more accurate. However, Wessel & Watts (1988) typically found the crossover difference among shipboard profiles of this vintage to be 5–10 mGal at these latitudes. These values are consistent with random errors of 3.5–7.1 mGal in each of the crossing shipboard gravity and the satellite gravity can be attributed to errors in the shipboard measurements although this suggestion cannot be confirmed. Of course, modern shipboard gravity measurements have achieved submGal accuracy through improved navigation and instrumentation (Bell & Watts 1985). Accurate shipboard gravity measurements were recently obtained in the Antarctic and it would

be important to compare the Geosat gravity field with the more accurate data.

These accuracy estimates are consistent with other recent studies. Bell *et al.* (1990) compared a Geosat gravity anomaly field based on just the ERM profiles with gravity anomalies derived from an airborne survey. In areas where the two data sets overlap, they have an rms difference of 7.3 mGal. They concluded that both data sets have accuracies of several mGal and resolutions of 20–30 km. Another comparison of gravity derived from 17 Geosat/ERM profiles in the Gulf of Mexico (~80 km track spacing) with complete shipboard gravity coverage shows an rms difference of 6.5 mGal; no DC adjustment is required (Small & Sandwell 1992). In this case Geosat gravity profiles were derived from single Geosat/ERM vertical deflection profiles using a 1-D approximation to equation (28). The long wavelengths were constrained by a spherical harmonic gravity model, complete to degree and order 180 (Rapp & Pavlis 1990). The dense shipboard gravity survey in the Gulf of Mexico (~2 km track spacing) contained better short-wavelength resolution, especially in shallow areas where the anomalies are not significantly attenuated by upward continuation from the seafloor. A cross-spectral analysis between the 17 coincident ship gravity and Geosat-derived gravity profiles shows significant coherence (>0.5) for wavelengths greater than 25 km; at a wavelength of 50 km the coherence is 0.95. The main limitation in recovery of the gravity field from widely spaced Geosat/EMS profiles is an incomplete knowledge of the cross-track vertical deflection. The implication is that the higher density of Geosat/GM coverage provides an alternative method of measuring marine gravity anomalies for wavelengths greater than about 25 km.

Preliminary tectonic interpretation

While the major tectonic and topographic features apparent in these gravity maps were also observed in the Geosat/ERM profiles (Sandwell & McAdoo 1988; Royer *et al.* 1990), the higher density Geosat data reveal some previously unknown features. Starting at 20° longitude and working east, the previously charted Gunnerus Ridge extends from the Antarctic margin at 32° longitude (Fig. 6a). The new data reveal a series of subtle lineations lying to the north and east of the Gunnerus Ridge. At 50° longitude, the northwest trending lineations, just seaward of the continental slope, may reflect the earliest stage of opening between India and Antarctica. These lineations appear to bend toward the northeast perhaps reflecting changes in relative motion between India and Antarctica.

Unfortunately, the evidence for fracture zone anomalies is less clear between 55° and 105° longitude (Figs 6a and b). The tectonic history of this seafloor between the Kerguelen Plateau and East Antarctica is still almost completely unknown. Further to the east (Fig. 6c), the gravity expressions of the Tasman and Balleny FZ's are readily apparent and show multiple strands of the Tasman FZ not seen previously.

The most important features apparent in the new gravity maps occur along the plate boundaries dividing the Indo–Australian, Antarctic and Pacific Plates. The trends of fracture zones on the flank of the Pacific–Antarctic Rise reveal the changes in spreading direction that are important for understanding the tectonics of the region. A good example is a major fracture zone crossing the ridge axis at −64.5°–171°. To the southwest of this FZ the ridge axis appears as a gravity trough while to the northeast of the FZ the ridge axis is offset in a right lateral direction and the axis appears as a weak gravity high. The transform fault connecting the ridge segments is oriented in the northwest direction. On the older ridge flanks, the fracture zones are oriented in a more easterly direction. This change in trend is associated with a well-documented change in relative motion between the Pacific and Antarctic plates that occurred between 4 and 6 Myr ago (Mayes, Lawver & Sandwell 1990). What was not known previously was how this recent change in spreading direction affected the major right-lateral offset connecting the Pacific–Antarctic rise to the Southeast Indian ridge. Previous unpublished gravity maps (e.g. Haxby, personal communication) based on Geosat/ERM data revealed a diamond-shaped gravity high between 160° and 180° longitude. The new Geosat gravity field shows that the diamond shaped region consists of many minor ridges and transforms (Fig. 6c). The transforms are oriented along the present Pacific–Antarctic opening direction. It has been proposed (Marks, McAdoo & Sandwell 1991) that this diamond-shaped gravity high started as a 'leaky transform' (see Menard & Atwater 1968) and rapidly evolved into the series of minor ridges and transforms. Despite the abundance of evenly spaced, N–S trending bathymetric profiles crossing the diamond-shaped zone of opening, the geometry of these minor ridges and transform was previously unknown.

Perhaps the most remarkable discovery in the detailed Geosat gravity field is the gravity expression of several propagating rift wakes. The most prominent example occurs on the Pacific–Antarctic rise (Fig. 6c; −63°, −166). It consists of a V-shaped gravity trough with one arm oriented north and the other arm oriented east. There is a minor right-lateral offset in the spreading axis at the propagating rift tip. The gravity expression of this feature is only about 5 mGal. This provides another upper bound on the noise in the gravity maps, although the clarity of the propagating rift gravity expression suggests that the precision is better (i.e. 1–2 mGal). A second possible propagating rift wake occurs along the Pacific–Antarctic rise toward the southwest (Fig. 6c; −65°, −173.5). In contrast to the first propagating rift which is propagating toward the southwest, this feature appears to be propagating towards the northeast.

A third possible propagating rift wake occurs on the older part of the Antarctic plate between the Eltanin and Udintsev FZ's (Fig. 6d; −61° to −63°, −108°) but, of course, only one half of the wake lies in the area of detailed gravity coverage. This N–S trending gravity trough is about 400 km long. It terminates at its southern end at a fracture zone having no throughgoing expression. The intersection of these two features suggests that the propagating rift eliminated the age offset on the fracture zone.

Further to the east are many more detailed gravity expressions of previously undiscovered features. Perhaps the most interesting is the herringbone pattern discovered in the Weddell Sea by Haxby (1988). He proposed that these features are gravity expressions of regularly spaced fracture zones associated with two spreading directions. Using a combination of airborne gravity measurements and Geosat/ERM profiles, Bell *et al.* (1990) have produced a

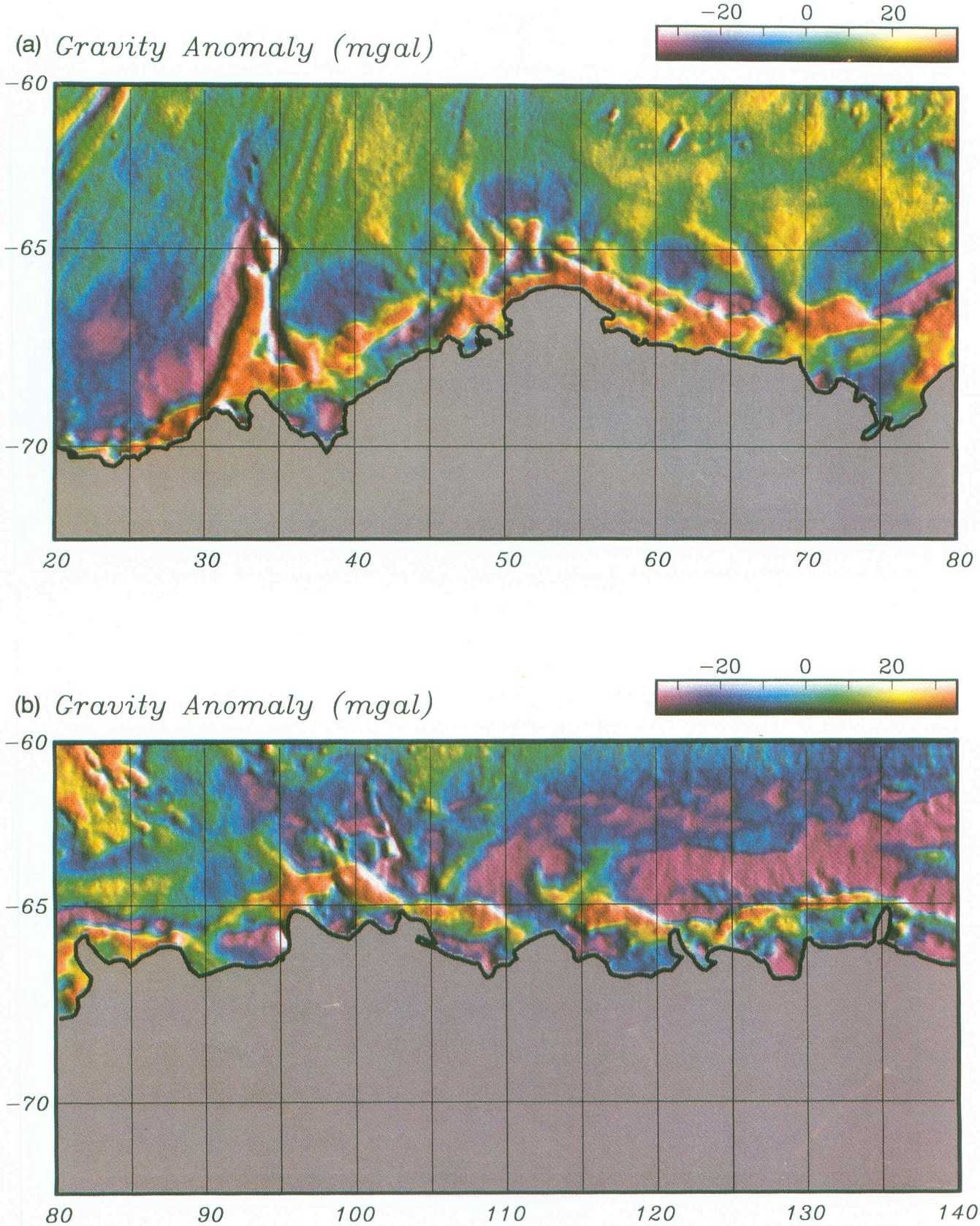

Figure 6. Gravity anomaly images. Violet represents anomalies −35 mGal or less while red–orange represents anomalies greater than 35 mGal. Images are shaded (80° azimuth) to highlight short-wavelength anomalies. Data were gridded on a Mercator projection with an x-spacing of 1/12° longitude and a y-spacing of 1/12° cos θ latitude.

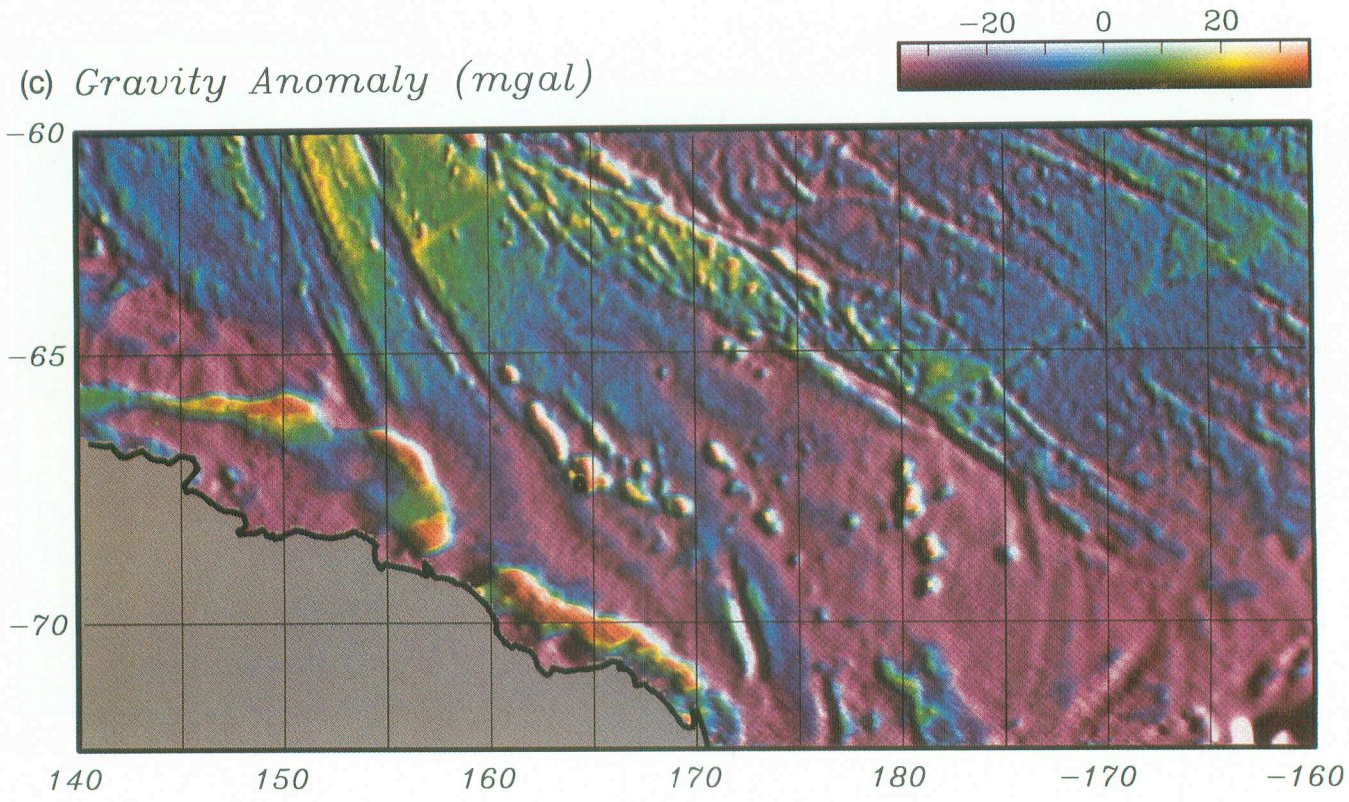

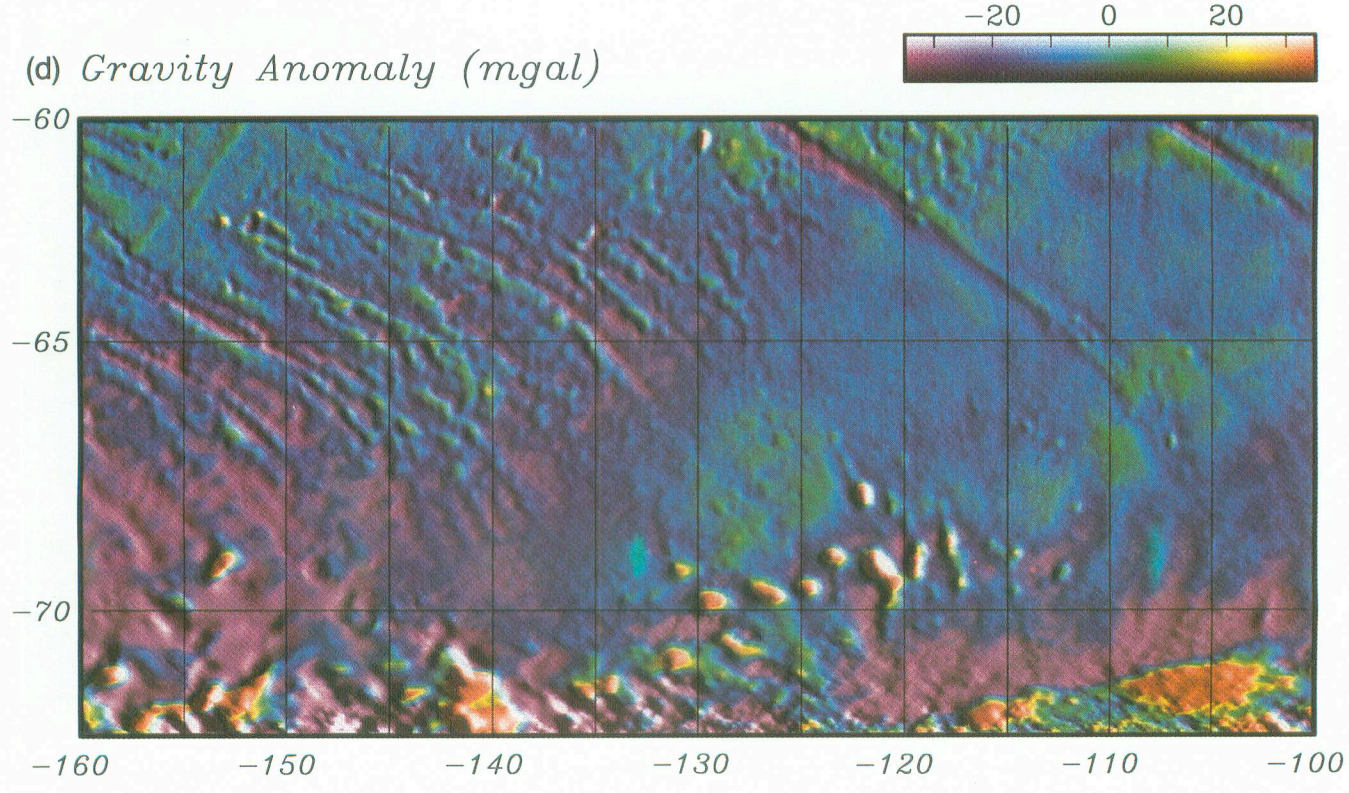

Figure 6. (*continued*)

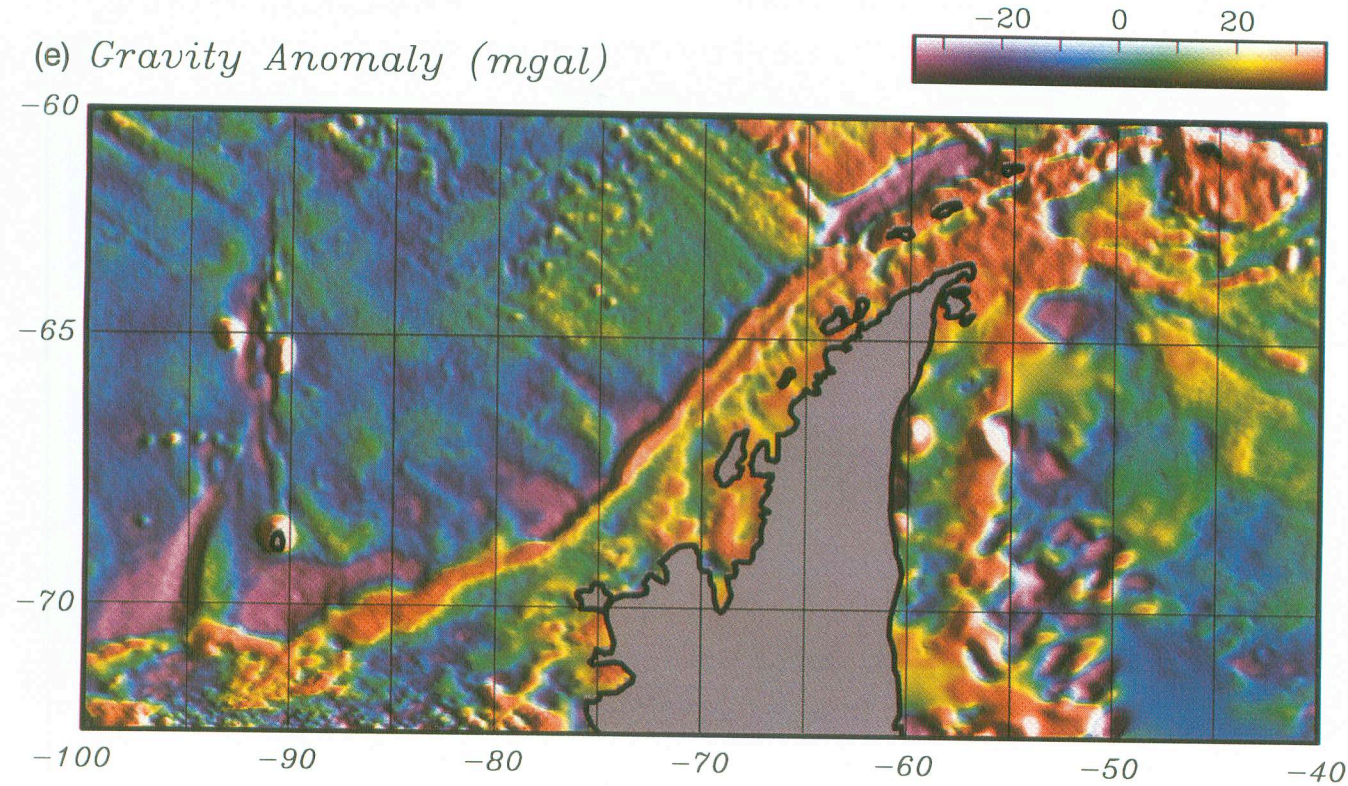

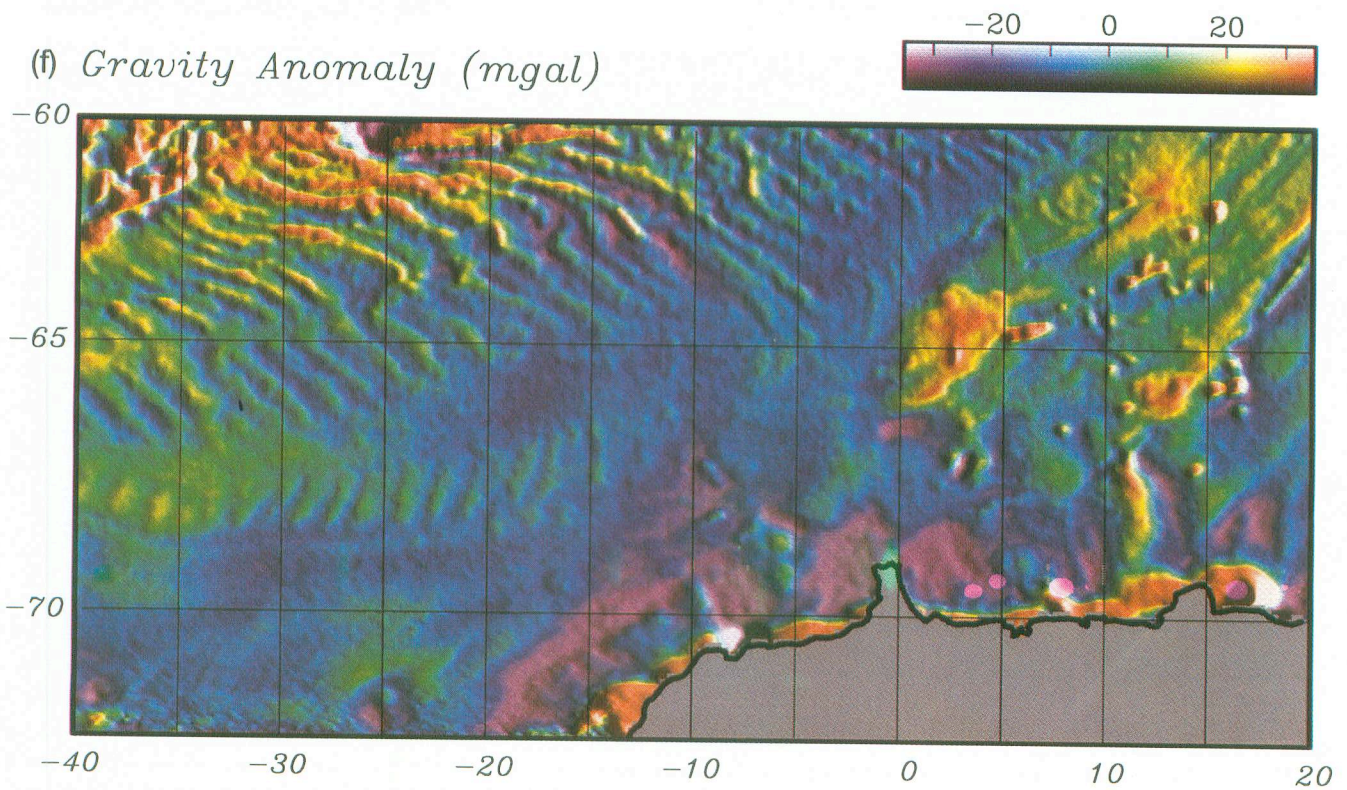

Figure 6. (*continued*)

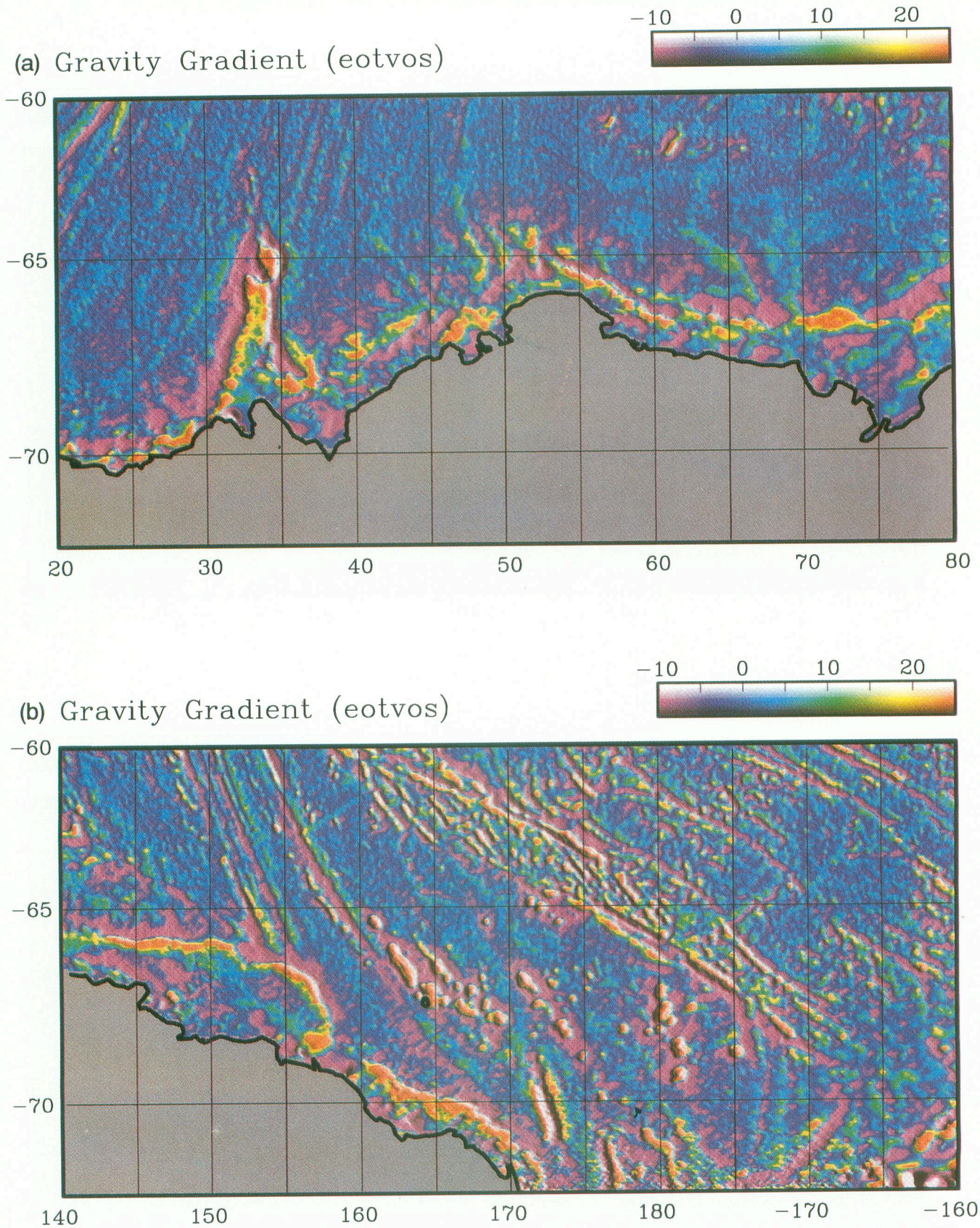

Figure 7. Gravity gradient images of (a) the East Antarctic Margin and (b) the Pacific–Antarctic Rise where violet represents anomalies of −10 Eötvös or less and red–orange represents anomalies of 25 Eötvös or more. The gravity gradient enhances the short-wavelength signatures associated with the tectonic fabric. It is computed directly from the original profiles using equation (23) so there are no edge effects near shorelines.

high-quality gravity map of the Western Weddell Sea showing the locations of the Larsen margin, which was incorrectly located by 100 km on previous maps, and the Ronne margin.

One could continue to speculate on the origins of all of the features seen in these gravity maps. However, convincing interpretations will require detailed tectonic modelling and such models are beyond the scope of this investigation. The important conclusion of this study is that accurate gravity maps can be constructed from high-density satellite altimeter measurements. The data analysis involves a number of simple processing steps that can be performed on a small computer having a large disc area. The only limitation to construction of detailed gravity maps in the remaining ocean areas is sparse data coverage.

ACKNOWLEDGEMENTS

I thank Bruce Douglas, Bob Cheney, Laury Miller, Russel Agreen, Dave McAdoo, John Bossler and others at the National Geodetic Survey for their efforts in obtaining, generating, and distributing the Geosat geophysical data records. Many of the methods and ideas used in this paper were obtained through discussions with Bill Haxby, Jim Marsh, Bruce Douglas, Tom Davis, Dave McAdoo, Dick Rapp, Bill Menke and others. In particular, Bill Haxby pioneered the display and gridding methods. Dick Rapp provided the code for generating geoid height and gravity anomaly from spherical harmonic coefficients. Research was supported by the NASA Solid Earth Sciences programme under grant NAG 1266 and the Defense Mapping Agency, Defense Hydrographic Initiative (ONR N00014-91-J-1642).

REFERENCES

Baudry, N., Diament, M. & Albouy, Y., 1987. Precise location of unsurveyed seamounts in the Austral archipelago area using Seasat data, *Geophys. J. R. astr. Soc.*, **89,** 869–888.

Bell, R. & Watts, A. B., 1985. Evaluation of the BGM-3 sea gravimeter system on board the *R/V Conrad, Geophysics*, **51,** 1480–1493.

Bell, R. E., Brozena, J. M., Haxby, W. F. & LaBrecque, J. L., 1990. Continental margins of the western Weddell sea: Insights from airborn gravity and Geosat-derived gravity, *Contrib. Antarctic Res. I, Antarctic Res. Ser.*, **50,** 91–102.

Bostrom, R. C., 1989. Subsurface exploration via satellite—structure visible in Seasat images of North Sea, Atlantic Continental Margin and Australia, *AAPG Bull.*, **73,** 1053–1064.

Calmant, S., Francheteau, J. & Cazenave, A., 1990. Elastic layer thickening with age of the oceanic lithosphere: a tool for prediction of the age of volcanoes or oceanic crust, *Geophys. J. Int.*, **100,** 59–67.

Cheney, R. E., Douglas, B. C., Agreen, R. W., Miller, L. L., Porter, D. L. & Doyle, N. S., 1987. Geosat altimeter geophysical data record user handbook, *NOAA Tech. Mem., NOS NGS-46.*

Freedman, A. P. & Parsons, B., 1986. Seasat-derived gravity over the Musician Seamounts, *J. geophys. Res.*, **91,** 8325–8340.

Haxby, W. F., 1987. *Gravity Field of the World's Oceans,* National Geophysical Data Center, NOAA, Boulder, CO.

Haxby, W. F., 1988. Organization of oblique sea floor spreading into discrete, uniformly spaces ridge segments: Evidence from Geosat altimeter data in the Weddell sea, *EOS, Trans. Am. geophys. Un.*, **69,** 1155.

Haxby, W. F. & Weissel, J. K., 1986. Evidence for small-scale mantle convection from Seasat altimeter data, *J. geophys. Res.*, **91,** 3507–3520.

Haxby, W. F., Karner, G. D., LaBrecque, J. L. & Weissel, J. K., 1983. Digital images of combined oceanic and continental data sets and their use in tectonic studies, *EOS, Trans. Am. geophys. Un.*, **64,** 995–1004.

Heiskanen, W. A. & Moritz, H., 1967. *Physical Geodesy,* Freeman, San Francisco.

Kaula, W. K., 1966. *Theory of Satellite Geodesy,* Blaidsel, Waltham, MA.

Marks, K. M. & Sailor, R. V., 1986. Comparison of Geos-3 and Seasat altimeter resolution capabilities, *Geophys. Res. Lett.*, **13,** 697–700.

Marks, K. M., McAdoo, D. C. & Sandwell, D. T., 1991. Geosat GM data reveal new details of ocean floor, *EOS, Trans. Am. geophys. Un.*, **72,** 145–149.

Marsh, J. G., Brenner, A. C., Beckley, B. D. & Martin, T. V., 1986. Global mean sea surface based upon Seasat altimeter data, *J. geophys. Res.*, **91,** 3501–3506.

Marsh, J. G., Koblinsky, C. J., Lerch, F., Klosko, S. M., Robbins, J. W., Williamson, R. G. & Patel, G. B., 1990. Dynamic sea surface topography, gravity and improved orbit accuracies from the direct evaluation of Seasat altimeter data, *J. geophys. Res.*, **95,** 13 129–13 150.

Mayes, C. L., Lawver, L. A. & Sandwell, D. T., 1990. Tectonic history and new isochron chart of the South Pacific, *J. geophys. Res.*, **95,** 8543–8567.

McAdoo, D. C., 1990. Gravity field of the southeast Central Pacific from Geosat exact repeat mission data, *J. geophys. Res.*, **95,** 3041–3047.

McAdoo, D. C. & Marks, K. M., 1992. High resolution marine gravity fields from Geosat Geodetic Mission, *J. geophys. Res.*, in press.

McAdoo, D. C., Martin, C. F. & Poulose, S., 1985. Seaset observations of flexure: Evidence for a strong lithosphere, *Tectonophysics*, **116,** 209–222.

McAdoo, D. C., Agreen, R. W., Cheney, R. E., Douglas, B. C., Doyle, N. S., Marks, K. M., Miller, L. & Timmerman, E. L., 1991. Geosat/Geodetic Mission geophysical data records: Format and contents, *NOAA Tech. Memo.*, in press.

Menard, W. H. & Atwater, T. M., 1968. Changes in direction of sea floor spreading, *Nature*, **219,** 463–467.

Menke, W., 1991. Applications of the POCS inversion method to interpolating topography and other geophysical fields, *Geophys. Res. Lett.*, **18,** 435–438.

Menke, W., Friberg, P., Lerner-Lam, A., Simpson, D., Bookbinder, R. & Karner, G., 1991. Sharing data over the Internet with the Lamont view-server system, *EOS, Trans. Am. Geophys. Un.*, **72,** 409–414.

Rapp, R. H. & Pavlis, N. K., 1990. The development and analysis of geopotential coefficient models to spherical degree 360, *J. geophys. Res.*, **95,** 21 885–21 991.

Roest, W. R., 1987. Seafloor spreading pattern of the North Atlantic between 10° and 40°N, *Geologica Ultraiectina*, **48,** 1–21.

Royer, J.-Y., Gahagan, L. M., Lawver, L. A., Mayes, C. L., Nurnberg, D., Sandwell, D. T. & Scotese, C. R., 1990. A tectonic chart of the Southern Ocean derived from Geosat altimeter data, *Antarctica as an Exploration Frontier—Hodrocarbon Potential, Geology and Hazards,* AAPG Studies in Geology No. 31, ed. John, B. S., Tulsa, OK.

Sailor, R. V. & LeSchack, A. R., 1987. Preliminary determination of the Geosat radar altimeter noise spectrum, *Johns Hopkins APL Technical Digest*, **8,** 182–183.

Sandwell, D. T., 1984a. A detailed view of the South Pacific from satellite altimetry, *J. geophys. Res.*, **89,** 1089–1104.

Sandwell, D. T., 1984b. Along-track deflection of the vertical from Seasat: GEBCO overlays, *NOAA Tech. Memo.*, NOS NGS-40.

Sandwell, D. T. & McAdoo, D. C., 1988. Marine gravity of the Southern Ocean and Antartic margin from Geosat, *J. geophys. Res.*, **93,** 10 389–10 396.

Sandwell, D. T. & Zhang, B., 1989. Global mesoscale variability from the Geosat exact repeat mission: Correlation with ocean depth, *J. geophys. Res.*, **94,** 17 971–17 984.

Sandwell, D. T. & McAdoo, D. C., 1990. High-accuracy, high-resolution gravity profiles from 2 years of the Geosat exact repeat mission, *J. geophys. Res.*, **95,** 3049–3060.

Shaw, P. R. & Cande, S. C., 1990. High-resolution inversion for South Atlantic plate kinematics using joint altimeter and magnetic anomaly data, *J. geophys. Res.*, **95,** 2625–2644.

Small, C. & Sandwell, D. T., 1989. An abrupt change in ridge axis gravity with spreading rate, *J. geophys. Res.*, **94,** 17 383–17 392.

Small, C. & Sandwell, D. T., 1992. A comparison of satellite and shipboard gravity measurements in the Gulf of Mexico, *Geophysics,* in press.

Wessel, P. & Watts, A. B., 1988. On the accuracy of marine gravity measurements, *J. geophys. Res.*, **93,** 393–413.

Wessel, P. & Haxby, W. F., 1990. Thermal stresses, differential subsidence, and flexure at oceanic fracture zones, *J. geophys. Res.*, **95,** 393–413.